JOURNAL OF APPLIED PHYSICS **123**, 095109 (2018)

Temperature-dependence of stress and elasticity in wet-transferred graphene membranes

Roberto De Alba,[1] T. S. Abhilash,[1] Aaron Hui,[2] Isaac R. Storch,[1] Harold G. Craighead,[2] and Jeevak M. Parpia[1,a)]
[1]*Department of Physics, Cornell University, Ithaca, New York 14853, USA*
[2]*School of Applied and Engineering Physics, Cornell University, Ithaca, New York 14853, USA*

(Received 24 September 2017; accepted 3 February 2018; published online 5 March 2018)

We report measurements of the mechanical properties of two suspended graphene membranes in the temperature range of 80 K to 550 K. For this entire range, the resonant frequency and quality factor of each device were monitored continuously during cooling and heating. Below 300 K, we have additionally measured the resonant frequency's tunability via electrostatic force, and modeled this data to determine graphene's tension and elastic modulus; both of these parameters are found to be strongly temperature-dependent in this range. Above 300 K, we observe a resonant frequency (and therefore tension) minimum near room temperature. This suggests that the thermal expansion coefficient is positive for temperatures below roughly 315 K, and negative for higher temperatures. Lastly, we observe a large, reproducible hysteresis in the resonant frequency as our graphene devices are cycled between 300 K and 550 K. After returning to 300 K, the measured frequency evolves exponentially in time with a time constant of ∼24 h. Our results clash with expectations for pristine graphene membranes, but are consistent with expectations for composite membranes composed of graphene coated by a thin layer of polymer residue. *Published by AIP Publishing.*
https://doi.org/10.1063/1.5006332

I. INTRODUCTION

Despite theoretical work and numerical simulations predicting that suspended graphene should expand as its temperature is lowered (i.e., it should have a negative thermal expansion coefficient, or TEC),[1,2] experimental graphene nanoelectromechanical systems (NEMS) have consistently shown increasing resonant frequencies as they are cooled below 300 K (Refs. 3–5)—suggestive of increased tension and a positive TEC. In some cases, this apparent discrepancy has been attributed to a large positive TEC of the metal at the membrane boundary,[3,4] but not all devices incorporate such a metal at the boundary. In most devices studied by our group—all of which have historically demonstrated positive TECs at and below 300 K—the graphene is supported on all sides by SiO_2 on Si, both of which have smaller TECs (in magnitude) than that expected theoretically for graphene.

Complicating matters further, graphene NEMS devices are generally expected to have a 1–2 nm layer of polymer residue on their surface. The polymer in question is usually poly(methyl methacrylate), commonly known as PMMA. For graphene grown by chemical vapor deposition (CVD), coating with a layer of ∼200 nm PMMA is part of a standard process used to remove the graphene from its growth substrate.[6,7] Graphene that has been exfoliated from bulk graphite is equally susceptible to contamination, since PMMA is typically used as a lithography resist in patterning metal electrodes on top of the exfoliated graphene.[3] While the vast majority of PMMA is easily removed by dissolving in acetone or another solvent, a small portion typically persists on the graphene surface. Even after high-temperature annealing in an H_2/Ar environment (a process specifically designed to remove PMMA from graphene), an almost full surface coverage of PMMA has been shown to persist.[8] This revelation is consistent with NEMS experiments that have attempted to measure the suspended membrane mass and typically produce a value that is 5–10 times larger than expected for clean monolayer graphene.[3,4,9]

In order for graphene to realize its potential as tunable, electrically conducting, atomically thin NEMS sensors of ultra-weak forces, masses, and displacements, the influence of surface contaminants and other non-idealities on its mechanical behavior must be fully understood. Similarly, because of the wide range of temperatures at which NEMS devices are employed, a better understanding of the temperature-dependence of graphene's structural properties is needed.

II. EXPERIMENT

A. Design

In order to measure the elastic properties of graphene, we suspended it over circular trenches in a Si/SiO_2 substrate, as shown in Fig. 1. This device geometry is functionally similar to graphene structures used in previous studies by our group.[9,10] Each device features three metallic electrodes (consisting of 5 nm Ti + 25 nm Pt) which serve as the Source, Drain, and Gate; the Source and Drain electrodes contact the graphene from underneath, while the Gate electrode is located at a distance $d = 1.3\,\mu$m below the graphene at the base of the circular trench. A voltage difference V is applied between the Drain and Gate electrodes (as depicted in Fig. 1) to induce static deformation and to excite resonant

---

[a)] jmp9@cornell.edu

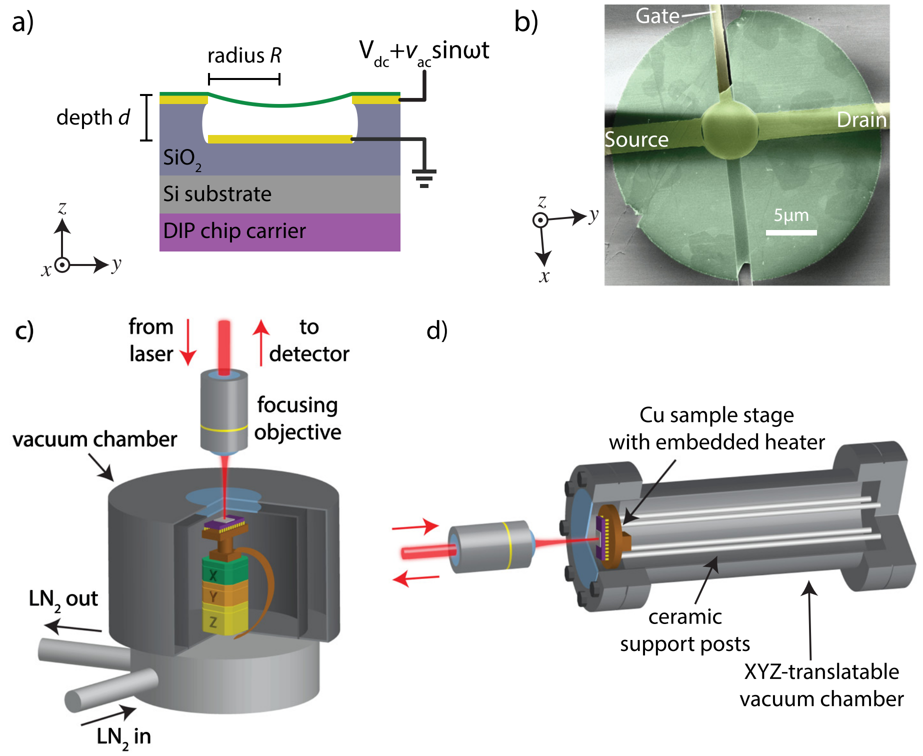

FIG. 1. Device and test chambers. (a) Cartoon diagram of a graphene device viewed in a cross-section. The suspended graphene (green) is pulled downward toward the metallic backgate via an applied voltage differential $V_{dc} + v_{ac} \sin \omega t$; the dc component V_{dc} stretches the graphene membrane, altering its tension and hence resonant frequency. (b) False-color SEM image of Device 1, showing the partially suspended graphene (green), metallic Source, Drain, and Gate electrodes (yellow), and the surrounding SiO$_2$ substrate (grey). (c) and (d) Experimental test chambers. (c) Liquid N$_2$ flow cryostat with optical access. Visible are the vacuum chamber and concentric inner radiation shield. The sample is mounted on a 24-pin Dual In-line Package (DIP, purple). (d) The high-temperature test chamber with the optical window. The DIP is seen here mounted on a Cu sample stage.

motion. The electrostatic force experienced by the graphene is $F = -(1/2)(dC/dz)V^2$, where dC/dz is the change in capacitance of the graphene-Gate system per unit vertical displacement of the graphene. The applied voltage can be separated into dc and ac components, $V = V_{dc} + v_{ac} \sin \omega t$, where t denotes time and ω is the applied drive frequency. Assuming $V_{dc} \gg v_{ac}$ (which holds for all of the present measurements), the static and time-varying forces on the membrane can be written as $F_{dc} = -(1/2)(dC/dz)V_{dc}^2$ and $F_{ac} = -(dC/dz)V_{dc}v_{ac}$.

The presence of both Source and Drain electrodes allows current to flow through the graphene, which can be useful for current-annealing[11] to remove surface contaminants (e.g., PMMA residue) or for utilizing the graphene transconductance—i.e., the change in conductance G per unit displacement relative to the Gate electrode dG/dz—to readout membrane motion.[12] However, neither of these was employed in this work. Current annealing acts primarily through ohmic heating, and was rejected here in favor of controlled heating of our devices in a custom-built high-temperature sample stage. Furthermore, membrane motion was detected using an all-optical method. This method is more sensitive than the transconductance measurement and does not suffer from the large "background" capacitive signal that often dominates the transconductance resonance signal. Optical detection for graphene NEMS has been described in previous studies, and is akin to optical interferometry.[9,10] A focused laser beam is incident on the device, and reflected light is collected by a high-speed photo-detector. Because of the graphene's 2.3% optical absorption, it encodes its displacement relative to the Gate (which acts as a static mirror) in the intensity of the reflected laser beam.

B. Device fabrication

We focus primarily on two graphene devices throughout this work: Device 1, with radius $R = 2.9\,\mu$m, and Device 2, with $R = 2.3\,\mu$m. A Scanning Electron Microscopy (SEM) image of Device 1 is shown in Fig. 1(b). Graphene for these devices was grown on Cu foil via CVD, and transferred to the pre-patterned substrate via standard processes.[9,10,13] Namely, the as-grown graphene was coated with 150 nm of PMMA, followed by wet etching of the Cu foil, cleaning of the graphene in deionized water, and wet transfer onto the prefabricated device substrate. The graphene (with the PMMA film still present) was then coated with photoresist and patterned to the $\sim 25\,\mu$m circular region shown using optical lithography and plasma etching. Finally, the PMMA and photoresist layers were removed by soaking in Microposit Remover 1165 (1-methyl-2-pyrrolidine) at 80 °C, followed by critical point drying in isopropyl alcohol to gently remove the devices from solution. Devices 1 and 2 originate from the same CVD graphene growth, and are located on the same substrate (a roughly 1 cm^2 Si chip).

C. Experimental apparatus

Diagrams of our experimental setup are shown in Figs. 1(c) and 1(d). Two separate test chambers are used to study the low-temperature (80–300 K) and high-temperature (300–550 K) behavior of our graphene membranes. For low-temperature measurements [Fig. 1(c)], an open-loop flow cryostat is employed. The graphene sample is located inside a vacuum chamber with optical access, and is mounted on piezo-electric translation stages in order to focus the detection laser directly on the desired device. The sample is thermally linked directly to the "cold finger" at the base of the cryostat via a braided Cu wire. For high-temperature measurements [Fig. 1(d)], the sample is mounted on a Cu stage which has an embedded resistive heater and is thermally isolated from the walls of the test chamber by ceramic support posts. In both test chambers, the ambient pressure is maintained below 10^{-6} Torr by an external ion pump.

D. Procedure

At a given temperature, we can measure the elastic properties of a graphene membrane by measuring its resonant frequency as a function of the applied electrostatic force F_{dc}. This applied force pulls the graphene towards the Gate, stretching it, and thereby increasing its tension by an amount commensurate with its Young's modulus and the induced strain. The resonant frequency of a circular membrane is given by $\omega_0 = (\alpha/R)\sqrt{\sigma/\rho}$, where α is a dimensionless constant and R, σ, and ρ are the membrane radius, tension, and mass per unit area, respectively. The tension is a combination of intrinsic tension σ_0 and electrostatically induced tension $\Delta\sigma = (1/2)Eh(\Delta A/A)$, where $\Delta A/A$ is the fractional change in surface area due to deflection, h is the membrane thickness, and $E = Y/(1-\nu^2)$ is the in-plane modulus. Here, Y and ν are the membrane Young's modulus and Poisson ratio. We will henceforth refer to the combination Eh as the 2-Dimensional (2D) modulus. For pristine graphene, the material parameters are $\rho = 0.75\ \mathrm{kg/m^2}$ and $Eh = 340\ \mathrm{N/m}$ (Ref. 14). These values cannot be assumed for our devices because of non-idealities such as surface contaminants and multi-grain CVD graphene.

If the applied voltage V_{dc} is varied over a large enough range, the three parameters ρ, σ_0, and Eh can be extracted from a polynomial fit of the type $\omega_0^2 = a + bV_{dc}^2 + cV_{dc}^4$. Expressed in terms of physical parameters, this is

$$\omega_0^2 = \left(\frac{\alpha}{R}\right)^2 \frac{\sigma_0}{\rho} - \frac{\epsilon_0 V_{dc}^2}{\rho d^3} + \frac{\beta E h \epsilon_0^2 V_{dc}^4}{\rho d^4 \sigma_0^2}, \tag{1}$$

where β is a dimensionless constant and ϵ_0 is the permittivity of free space. The V_{dc}^0 and V_{dc}^4-order terms in this expression describe a tensioned membrane under electrostatic load as described above, and the V_{dc}^2-order term represents a nonlinear dynamics effect known as capacitive softening. This is caused by modulation of the graphene-Gate capacitance (and hence the applied force F_{dc}) as the membrane vibrates. The gradient of this force dF_{dc}/dz acts as a negative spring constant, reducing the resonant frequency. This effect is common in capacitively driven NEMS structures. Although all membrane modes will in theory obey Eq. (1), we focus solely on the fundamental mode, where $\alpha \approx 2.4048$ and $\beta \approx 0.1316$. A derivation of Eq. (1) is provided in the supplementary material.

Shown in Fig. 2(a) is a sample data set for Device 2 measured at 300 K. Here, the vibration amplitude (in units of μV produced by the photo-detector) is measured as a function of drive frequency and V_{dc}, where V_{dc} is the slow scan axis. We note that in order to obtain an adequate signal to noise ratio, the membrane is in some cases driven into the nonlinear "Duffing" regime. That is, the amplitude of motion is sufficiently large that the measured linescans are strongly asymmetric [Figs. 2(c) and 2(d)]; this is consistent with motion-induced membrane stiffening, as it always displays spring hardening (i.e., a right-leaning peak). From these

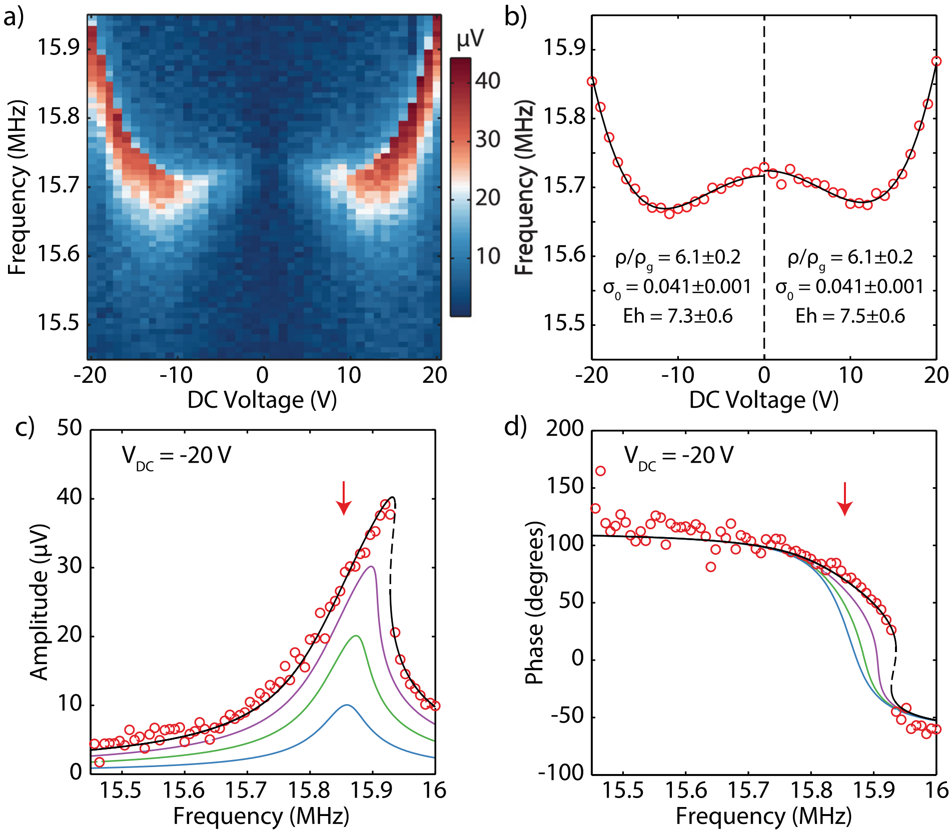

FIG. 2. A sample V_{dc} scan of Device 2, measured at 300 K. (a) Amplitude of graphene motion vs drive frequency and V_{dc}. (b) The extracted resonant frequencies $\omega_0/2\pi$ from (a) (circles), and fits to the model described in the text (black lines). (c) and (d) A single linescan from (a) taken at $V_{dc} = -20$ V (circles), plotted as amplitude and phase. The red arrows indicate the location of the resonant frequency, as determined from a Duffing model fit to the data (black lines). The colored lines are theoretical linescans using the same Duffing constant, but weaker drive forces. The dashed portions of the fit indicate multivalued regions. The details of the Duffing model fit are provided in the supplementary material.

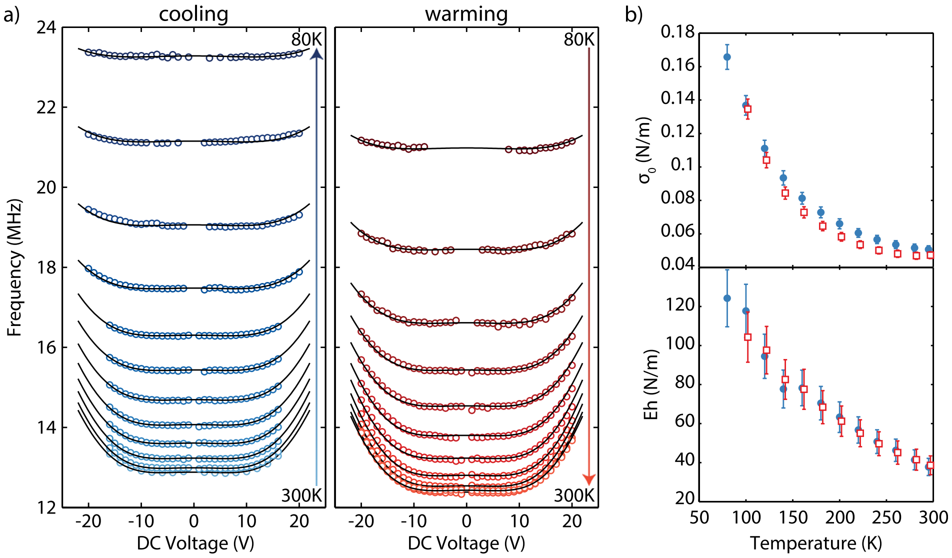

FIG. 3. Low-temperature frequency measurements of Device 1. (a) Measured resonant frequencies $\omega_0/2\pi$ (circles) versus V_{dc} at multiple temperatures during cooling (left panel) and warming (right panel). The black lines are the fits to the data at each temperature, using averaged fit parameters from separate fits to the $V_{dc} < 0$ and $V_{dc} > 0$ ranges. (b) The membrane intrinsic tension σ_0 and modulus Eh extracted from the fits in (a). The filled circles are data taken during cooling, and the open squares are data taken during warming.

nonlinear linescans, a fit to the phase and amplitude (black lines) allows us to extract the true resonant frequency, which does not coincide with the peak amplitude. In this way, the resonant frequency ω_0 is measured at each voltage V_{dc} and fitted to a modified version of Eq. (1), as shown in Fig. 2(b); the full fitting model substitutes the total tension $\sigma = \sigma_0 + \Delta\sigma$ into the denominator of the V_{dc}^4 term, producing better results at high V_{dc}, while maintaining only three free-parameters ρ, σ_0, and Eh. See the supplementary material for more details. In fitting the resonant frequencies [black lines in Fig. 2(b)], positive and negative V_{dc} data are fitted separately to allow for slight temperature variations over the slow V_{dc} scan, and fit parameters are then combined in an inverse-variance weighted average. Uncertainties in the resulting parameters ρ, σ_0, and Eh reflect 68% confidence intervals based on the residuals of the fits.

III. RESULTS

Low-temperature data for Devices 1 and 2 is shown in Figs. 3 and 4. In both cases, the sample temperature T was lowered from 300 K to 80 K in 20 K increments and then returned to 300 K at the same rate. As can be seen in both data sets, the ω_0 versus V_{dc} curves shift upward in frequency and flatten considerably as the temperature is decreased below 300 K. Because of the flattening of this data, the 3-parameter fit for ρ, σ_0, and Eh described above becomes increasingly unreliable at low temperatures. To counteract this, the 3-parameter fit was performed only initially at $T = 300$ K, and the resulting mass density ρ was used in a 2-parameter fit at all lower temperatures. The assumption that ρ remains constant over the entire temperature range is justified because: (1) a constant vacuum is maintained throughout the experiment, so any adsorption or desorption of gases from the membrane surface is minimal. (2) The membrane is far from the coldest component of the cryostat, meaning that any potential cryopump effect that could lead to increased gas and mass adsorption is also negligible. Because our fitted value of ρ at 300 K has some associated uncertainty, a Monte-Carlo approach was used in the 2-parameter fits (each fit was performed 500 times using random, normally distributed ρ values) to estimate the error bars for σ_0 and Eh.

The measured mass of each device at $T = 300$ K is (in units of graphene monolayers): $\rho = 7.2 \pm 0.5$ for Device 1

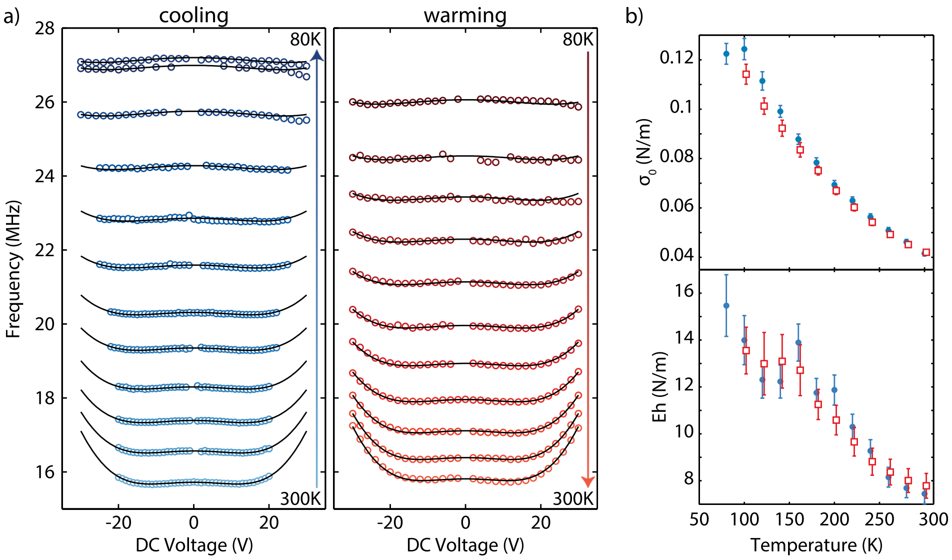

FIG. 4. Low-temperature frequency measurements of Device 2. (a) and (b) Similar results to the previous figure, taken using Device 2.

and $\rho = 6.1 \pm 0.2$ for Device 2. Using these masses, the fits to the low-temperature data produce the values of σ_0 and Eh shown in Figs. 3(b) and 4(b). Both devices show a monotonic increase in σ_0 and Eh as the temperature decreases. We note that this increase in σ_0 is counter to expectations for ideal graphene, as its negative thermal expansion coefficient (TEC) of $\alpha_g \approx -4.8 \times 10^{-6}\,\mathrm{K}^{-1}$ (Ref. 2) should be large enough in magnitude to counter the thermal contraction of the surrounding Si substrate with $\alpha_{\mathrm{Si}} \approx 2.6 \times 10^{-6}\,\mathrm{K}^{-1}$ (Ref. 15). Furthermore, our measured values for Eh at 300 K are much smaller than the 340 N/m expected for ideal graphene. This incredible softening of CVD graphene has been studied previously in great detail, and is likely due to grain boundaries and nm-scale ripples in the membrane surface.[16,17] The variation in Eh between our two devices is also consistent with previous experiments.[17,18] As a final remark on Figs. 3 and 4, the observed upward trends in σ_0 and Eh at low temperatures agree well with unpublished measurements made on similar devices using static behavior rather than dynamics;[19] in that experiment, tension and modulus were measured by applying an electrostatic load and using a nonlinear model to fit the resulting force-displacement curve.

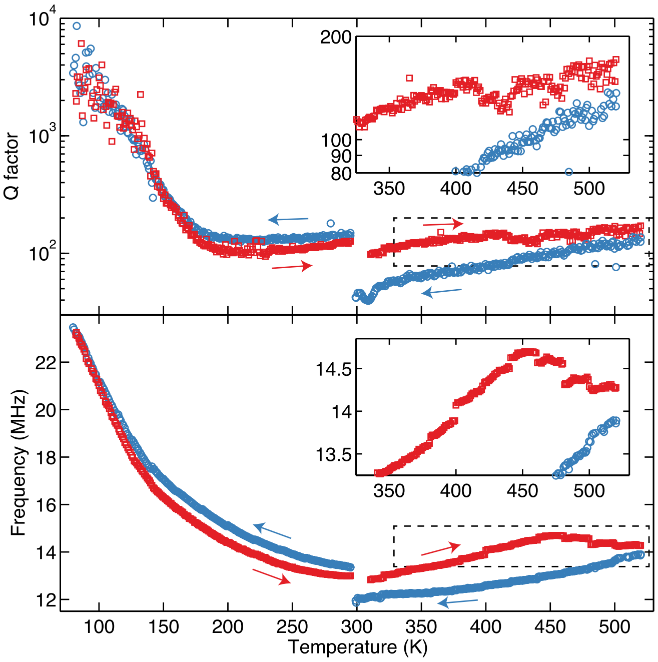

FIG. 5. Resonant frequency and Q of Device 1 over the entire temperature range. Red squares: data taken while warming. Blue circles: data taken while cooling. The arrows indicate the direction of the temperature ramp. Insets: magnified images of the dashed regions; these show "slipping events" caused by gate voltage V_{dc} scans at high temperatures, which are characterized by irreversible downward shifts in frequency and Q.

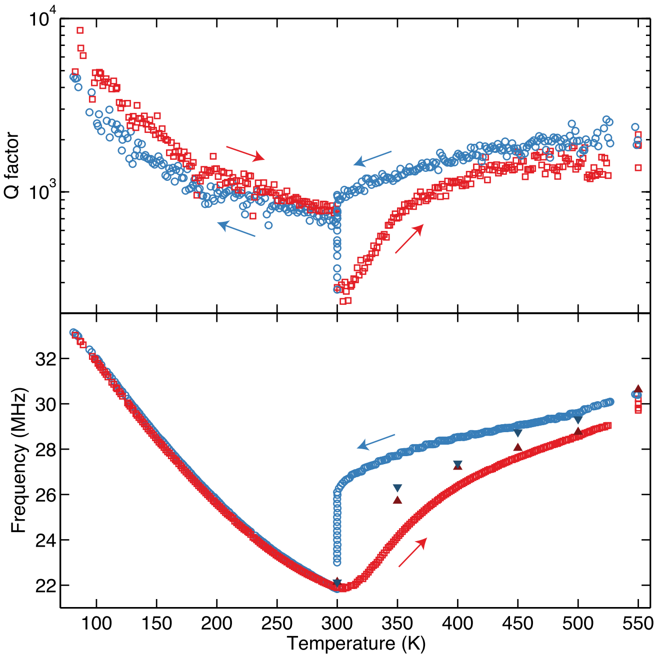

FIG. 6. Resonant frequency and Q of Device 2 over the entire temperature range. Red squares: data taken while warming. Blue circles: data taken while cooling. The arrows indicate the direction of the temperature ramp. Above 300 K, a continuous heating rate of 0.2 K/min was used. In the lower panel, the triangles represent saturation frequencies measured during a subsequent heating cycle in which the temperature was varied in 50 K increments; here, each temperature was held constant for several hours to allow the membrane to reach equilibrium. Upward (downward) triangles: saturation frequencies measured during heating (cooling).

The behavior of our devices within the entire temperature range of 80 K–550 K is summarized in Figs. 5 and 6. Here, the resonant frequency ω_0 and quality factor Q were measured (from continuously repeated linescans) using constant voltage V_{dc} as the temperature was varied. Both devices are located on the same substrate (i.e., the same Si chip), so although only one device could be monitored during any given temperature cycle, both devices share the same thermal history. The data below room temperature in Fig. 5 was measured along with data in Fig. 3, using a voltage of $V_{dc} = -16$ V. We observe greatly enhanced Q factors at low temperatures, consistent with previous experiments,[3,5] and slight hysteresis in ω_0 upon returning to 300 K. During heating to 520 K, V_{dc} sweeps were performed on Device 1 in 20 K increments in order to track its mechanical parameters (ρ, σ_0, and Eh) as was done at cryogenic temperatures. This, however, led to degradation of the resonant frequency and Q, as evidenced in Fig. 5. At the highest temperatures, downward shifts in frequency were observed immediately following each V_{dc} sweep, possibly due to slipping of the graphene on the substrate or to a conformational change of polymer contaminants on the graphene. The observed hysteresis upon returning to 300 K was irreversible, and the measured values of ρ, σ_0, and Eh during the cycle (not shown here) were erratic. Upon a second heating cycle to 550 K (not shown), Device 1 failed and was thereafter unusable.

The data shown in Fig. 6 for Device 2 was measured without intermediate V_{dc} sweeps; a constant voltage of $V_{dc} = 3$ V was maintained throughout. Considerable hysteresis is seen during the 300 K–550 K heating cycle, but this proved to be largely reversible. Multiple heating cycles at various heating rates produced similar results to those shown. We observed that when maintaining a fixed temperature (e.g., at 550 K or 300 K in Fig. 6), the resonant frequency (and the Q) of the membrane evolves exponentially in time as $\omega_0(t) - \omega_{\mathrm{sat}} \propto e^{-t/\tau}$, where ω_{sat} and τ are the saturation value and time constant, respectively. This is depicted in Fig. 7. In order to study this behavior further, a second

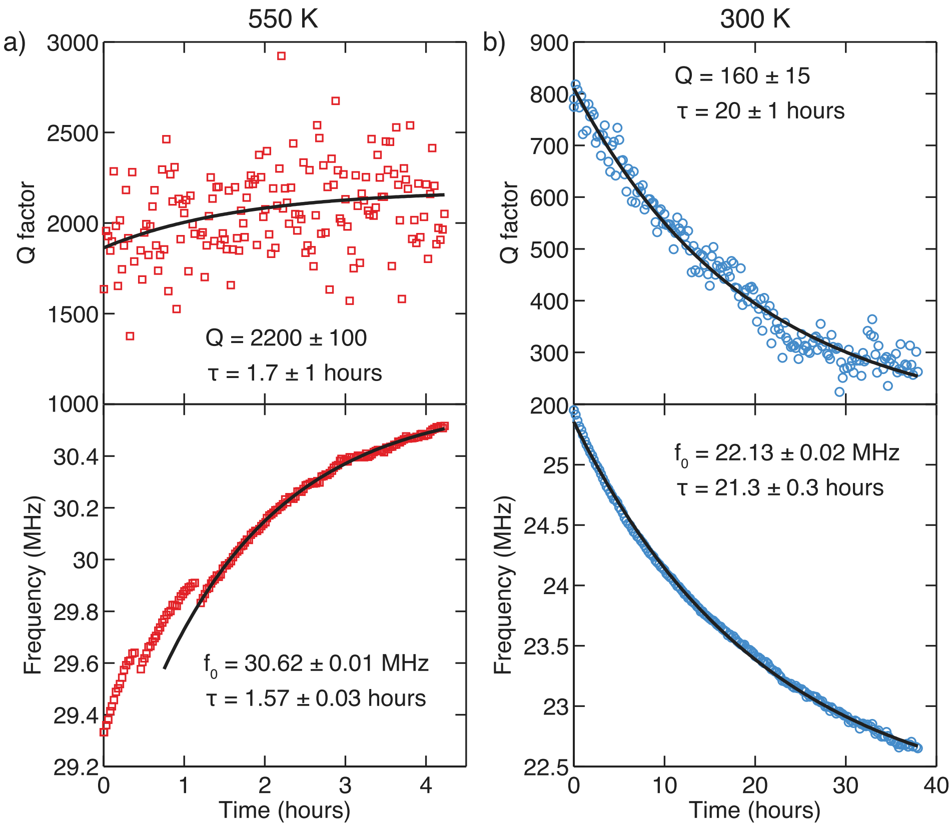

FIG. 7. Evolution of Device 2 at a fixed temperature. A portion of the frequency and Q data used to produce the saturation values (triangles) in Fig. 6. The values were continuously measured over time while maintaining a fixed temperature (a) at $T = 550$ K, and (b) after returning to room temperature $T = 300$ K. The black line in each panel is an exponential fit to the data, with saturation values and time constants τ as shown. In (a), abrupt jumps in frequency are caused by manual refocusing of the detection laser beam. Q factors are noticeably noisier in (a), partially due to operation far into the Duffing regime and possibly compounded by thermal fluctuations which resulted in noisy, hysteretic linescans. Linescans used to produce (b) demonstrated linear device operation; identical drive voltages were applied at both temperatures.

heating cycle was performed in which the temperature was varied in 50 K increments and maintained at each temperature for several hours. The resulting saturation frequencies are shown in Fig. 6, and display a near complete closing of the hysteresis loop. Interestingly, time constants measured during heating (upward triangles) were typically 1–2 h, while those measured during cooling (downward triangles) were typically 12–24 h.

We note that the data for Device 2 shown in Figs. 6 and 7 was taken after all measurements of Device 1 (meaning that the device had previously been cycled to 80 K and 550 K), but prior to the measurements shown in Fig. 4. In the intervening time between the measurements of Figs. 6 and 4 (12 weeks in total), the device was stored under vacuum and electrically grounded at $V_{dc} = 0$. Still, there was a marked change in resonant frequency at 300 K between measurements, the source of which remains unknown.

IV. DISCUSSION

There are several observed thermal effects in our two devices which are wholly unexpected for pristine graphene membranes. These include: (1) a non-monotonic resonant frequency as a function of temperature, (2) a strongly temperature-dependent 2D modulus Eh, and (3) long time constants for frequency relaxation after heating. We conjecture that all of these effects can be explained by a thin layer of polymer residue (most likely the PMMA used during fabrication) on the graphene surface. As mentioned earlier, a thin film (1–2 nm) of PMMA is known to persist on CVD graphene even after standard annealing methods are implemented to remove it.[8,20]

To elucidate this further, we can model our membranes as consisting of monolayer graphene with modulus, thickness, and TEC given by E_g, h_g, and α_g coated by a polymer film with corresponding parameters E_p, h_p, and α_p. The effective 2D modulus and TEC of the composite membrane can then be approximated as[21,22]

$$Eh = E_g h_g + E_p h_p, \tag{2}$$

$$\alpha = \frac{\alpha_g E_g h_g + \alpha_p E_p h_p}{E_g h_g + E_p h_p}. \tag{3}$$

Here, all the parameters E_g, E_p, α_g, and α_p are expected to be functions of temperature. The tension σ_0 of such a composite membrane would then depend on temperature as

$$\sigma_0(T) = E_g(T) h_g \varepsilon_{300\mathrm{K}} + E(T) h \int_{300\mathrm{K}}^{T} \left(\alpha(T') - \alpha_{\mathrm{Si}}(T')\right) dT'. \tag{4}$$

Here, $\varepsilon_{300\mathrm{K}}$ is the graphene strain at room temperature, and $\alpha_{\mathrm{Si}}(T)$ is the TEC of the surrounding substrate. For consistency with our experimental observations (discussed below), we have assumed in Eq. (4) that the polymer has zero strain at room temperature. Note that temperature-dependence of σ_0 arises not only due to thermal expansion, but also from the temperature-dependent moduli. Within our experimental temperature range of 80–550 K, the substrate expansion $\alpha_{\mathrm{Si}} \lesssim 3.7 \times 10^{-6}\,\mathrm{K}^{-1}$ (Refs. 15 and 23) is expected to be smaller in magnitude than either graphene or PMMA.

Using the reported values for the volumetric mass density,[24] modulus,[25] and TEC[26] of bulk PMMA ($1.1\,\mathrm{kg/m^3}$, $E_p = 3$ GPa, and $\alpha_p = 8 \times 10^{-5}\,\mathrm{K}^{-1}$ at room temperature), we can estimate the thickness of our polymer films and their contribution to the overall membrane TEC as given by Eq. (3). Undoubtedly, the material properties of PMMA can vary based on molecular weight and can differ between the bulk material and thin films, but this should suffice to give a qualitative explanation of our observations. The measured mass densities of our membranes of $\rho \approx 6$–7 graphene monolayers suggest the polymer films have thickness $h_p \approx 3$–$4\,\mathrm{nm}$. This would lead to a 2D modulus of $E_p h_p \approx 10\,\mathrm{N/m}$, which is comparable to the total moduli Eh we have measured [shown in Figs. 3(b) and 4(b)]. For both of our devices, this then suggests a 2D graphene modulus of $E_g h_g \lesssim 30\,\mathrm{N/m}$ at room temperature based on Eq. (2). Substituting these values for $E_p h_p$ and $E_g h_g$ into Eq. (3) (with $\alpha_p = 8 \times 10^{-5}\,\mathrm{K}^{-1}$ and $\alpha_g \approx -5 \times 10^{-6}\,\mathrm{K}^{-1}$ from literature[2,26]) then reveals that the TEC of PMMA should dominate the composite membrane TEC at room temperature. Furthermore, because the TEC and modulus of graphene are expected to remain roughly constant at low temperatures,[2] while for polymers (and PMMA specifically) the modulus is expected to rise,[27] the composite membrane should continue to have a TEC $\alpha > 0$ below 300 K. This is consistent with our measurements of $\sigma_0(T)$ and $\omega_0(T)$ as presented in Figs. 3–6, as well as our observed increase in Eh at low temperatures.

At some temperature $T > 300\,\mathrm{K}$, PMMA is expected to pass through its glass transition. During this transition, it changes from a rigid, glassy state to a soft, rubbery state; this is characterized by a sudden drop in Young's modulus E_p by up to three orders of magnitude.[27] Therefore, when our composite membrane passes through the glass transition temperature, its TEC $\alpha(T)$ should transition from being PMMA-dominated to graphene-dominated, and we should observe a sudden change from $\alpha > 0$ to $\alpha < 0$. For bulk PMMA, the glass transition temperature occurs at $T \approx 380\,\mathrm{K}$;[28] however, for PMMA and other polymers, this transition has been shown to shift to lower temperatures as the film thickness decreases.[29–33] We thus interpret the minimum in resonant frequency observed for Device 2 at $T \approx 315\,\mathrm{K}$ (in Fig. 6) as indicative of the PMMA passing through its glass transition, and giving way to the negative thermal expansion of graphene α_g at higher temperatures. Because this transition (and the inferred sudden drop in E_p) is not accompanied by a sharp downward frequency shift, we infer that the in-built strain $\varepsilon_{300\mathrm{K}}$ is present only in the graphene layer. That is to say, the PMMA layer has a negligible strain at 300 K. This is reflected in Eq. (4).

The hysteresis and long time constants seen in Figs. 6 and 7 are also consistent with polymer relaxation. The long time constants observed can be a sign of creep (i.e., very slow deformation) of the polymer in response to the ever-present tensile stress applied to it by the graphene—both in the glassy and rubbery states.[34–36] Particularly during cooling and vitrification (i.e., re-entering the glassy state), relaxation times in polymers are known to increase dramatically; timescales of several hours are common near the glass transition.[28,37] Because the polymer layers on our devices are only a few molecular chains thick and under constant tensile stress from the graphene, time constants for creep and relaxation may vary substantially from that expected of bulk PMMA. The previously mentioned downward shift in resonant frequency observed in Device 2 between Figs. 4 and 6 over 12 weeks may also be a result of aging of the PMMA.[38]

An alternate explanation for the long time constants observed in Device 2 above 300 K is that mass (e.g., trace gases in the vacuum chamber such as water vapor) is adsorbing onto or desorbing from the membrane surface—despite the low pressures $\sim 10^{-6}$ Torr used. Such an effect would be consistent with the slow rise in frequency at 550 K and the fall in frequency at 300 K shown in Fig. 7, as adsorbates leave the membrane at high temperatures and are re-adsorbed (at a much slower rate) at low temperatures. Attempts to discount this theory—by performing V_{dc} sweeps to measure ρ during the frequency relation at 300 K—have thus far been inconclusive. This effect may therefore contribute to the apparent negative TEC observed above 315 K, and further testing is needed. For the frequency decay observed in Fig. 7 at 300 K to be entirely adsorbate-driven, a change in frequency from 26 MHz to 22 MHz suggests a 40% mass increase (assuming tension is constant). Using the measured value of $\rho = 6.1$ monolayers in steady state at 300 K, this corresponds to an increase in mass of roughly 2 graphene monolayers.

Finally, we note that the potential presence of ripples on the graphene surface[16,17] could also play a role in the observed trends in modulus and tension. Indeed, it is unclear how such ripples would affect the membrane's dynamical behavior, or how the ripple amplitude would depend on the temperature and thermal history of the device. However, the long time constants observed in our devices—which we have attributed to PMMA relaxation—seemingly cannot be explained by ripples, as they should form near-instantaneously as the membrane temperature changes. Repeated measurements of the high-temperature data in Fig. 6) (not shown), suggest that no new ripples are formed during the heating cycle shown.

V. CONCLUSION

In summary, we have studied the mechanical properties of two tensioned CVD graphene membranes under vacuum in the temperature range of 80 K–550 K. We observe a number of behavioral responses of the membranes that are inconsistent with our expectations for pristine, single crystal graphene. Namely: (1) the measured mass density ρ corresponds to 6–7 times that of monolayer graphene. (2) The measured membrane tension σ_0 and 2D modulus Eh both increase as the temperature is decreased below 300 K, in contrast to the expectations of a negative TEC and constant modulus. (3) The resonant frequency has a minimum at $T \approx 315\,\mathrm{K}$. (4) The resonant frequency evolves with long time constants of 1–2 h during heating above room temperature, and 12–24 h while cooling back to room temperature. All of these observations are consistent with a thin 1–4 nm film of PMMA residue on the graphene surface, although the high temperature measurements may be confounded by desorption and adsorption of gasses in our high vacuum test chamber, or by ripples present on the graphene surface. These results indicate that while graphene mechanical resonators benefit from the low mass and electrical conductivity of graphene, many of the mechanical properties of these devices are ultimately dominated by polymer contaminants and other non-idealities. The loss modulus of PMMA may also play a dominant role in determining the Q factor of graphene devices, which are known to be substantially lower than most other resonating membrane systems.[39]

SUPPLEMENTARY MATERIAL

See supplementary material for a derivation of Eq. (1), additional information on fitting of the resonant frequency versus gate voltage, and details on the fitting algorithm used for Duffing resonance peaks. Also provided are alternative versions of Figs. 3(b) and 4(b) in which the mass density ρ was not held fixed but used as a third fitting parameter in addition to σ_0 and Eh.

ACKNOWLEDGMENTS

This work was supported in part by the Cornell Center for Materials Research with funding under DMR-1120296 and by the NSF under DMR-1202991 and DMR-1708341. We acknowledge the help of Eric Smith and Vivek Adiga for the design and assembly of the high temperature stage. We also thank Paul McEuen for many insightful discussions regarding the thermal properties of graphene. The devices were fabricated at the Cornell Nanoscale Facility, a member of the National Nanotechnology Coordinated Infrastructure (NNCI) supported by the NSF under ECCS-1542081.

[1] J.-W. Jiang, J.-S. Wang, and B. Li, Phys. Rev. B **80**, 205429 (2009).
[2] K. V. Zakharchenko, M. I. Katsnelson, and A. Fasolino, Phys. Rev. Lett. **102**, 046808 (2009).
[3] C. Chen, S. Rosenblatt, K. I. Bolotin, W. Kalb, P. Kim, I. Kymissis, H. L. Stormer, T. F. Heinz, and J. Hone, Nat. Nanotechnol. **4**, 861 (2009).
[4] V. Singh, S. Sengupta, H. S. Solanki, R. Dhall, A. Allain, S. Dhara, P. Pant, and M. M. Deshmukh, Nanotechnology **21**, 165204 (2010).
[5] A. M. van der Zande, R. A. Barton, J. S. Alden, C. S. Ruiz-Vargas, W. S. Whitney, P. H. Pham, J. Park, J. M. Parpia, H. G. Craighead, and P. L. McEuen, Nano Lett. **10**, 4869 (2010).
[6] A. Reina, X. Jia, J. Ho, D. Nezich, H. Son, V. Bulovic, M. S. Dresselhaus, and J. Kong, Nano Lett. **9**, 30 (2009).
[7] X. Li, Y. Zhu, W. Cai, M. Borysiak, B. Han, D. Chen, R. D. Piner, L. Colombo, and R. S. Ruoff, Nano Lett. **9**, 4359 (2009).
[8] Y.-C. Lin, C.-C. Lu, C.-H. Yeh, C. Jin, K. Suenaga, and P.-W. Chiu, Nano Lett. **12**, 414 (2012).
[9] R. A. Barton, I. R. Storch, V. P. Adiga, R. Sakakibara, B. R. Cipriany, B. Ilic, S. P. Wang, P. Ong, P. L. McEuen, and J. M. Parpia, Nano Lett. **12**, 4681 (2012).
[10] R. De Alba, F. Massel, I. R. Storch, T. S. Abhilash, A. Hui, P. L. McEuen, H. G. Craighead, and J. M. Parpia, Nat. Nanotechnol. **11**, 741 (2016).
[11] J. Moser, A. Barreiro, and A. Bachtold, Appl. Phys. Lett. **91**, 163513 (2007).
[12] Y. Xu, C. Chen, V. V. Deshpande, F. A. DiRenno, A. Gondarenko, D. B. Heinz, S. Liu, P. Kim, and J. Hone, Appl. Phys. Lett. **97**, 243111 (2010).
[13] X. Liang, B. A. Sperling, I. Calizo, G. Cheng, C. A. Hacker, Q. Zhang, Y. Obeng, K. Yan, H. Peng, and Q. Li, ACS Nano **5**, 9144 (2011).
[14] C. Lee, X. Wei, J. W. Kysar, and J. Hone, Science **321**, 385 (2008).
[15] Y. Okada and Y. Tokumaru, J. Appl. Phys. **56**, 314 (1984).
[16] W. Bao, F. Miao, Z. Chen, H. Zhang, W. Jang, C. Dames, and C. N. Lau, Nat. Nanotechnol. **4**, 562 (2009).
[17] C. S. Ruiz-Vargas, H. L. Zhuang, P. Y. Huang, A. M. van der Zande, S. Garg, P. L. McEuen, D. A. Muller, R. G. Hennig, and J. Park, Nano Lett. **11**, 2259 (2011).
[18] R. J. Nicholl, H. J. Conley, N. V. Lavrik, I. Vlassiouk, Y. S. Puzyrev, V. P. Sreenivas, S. T. Pantelides, and K. I. Bolotin, Nat. Commun. **6**, 8789 (2015).
[19] I. R. Storch, R. De Alba, V. P. Adiga, T. S. Abhilash, R. A. Barton, H. G. Craighead, J. M. Parpia, and P. L. McEuen, "Young's Modulus and Thermal Expansion of Tensioned Graphene Membranes" (unpublished).
[20] Y.-C. Lin, C. Jin, J.-C. Lee, S.-F. Jen, K. Suenaga, and P.-W. Chiu, ACS Nano **5**, 2362 (2011).
[21] M. R. Begley, H. Bart-Smith, O. N. Scott, M. H. Jones, and M. L. Reed, J. Mech. Phys. Solids **53**, 2557 (2005).
[22] I. Sevostianov, Mech. Mater. **45**, 20 (2012).
[23] T. Middelmann, A. Walkov, G. Bartl, and R. Schödel, Phys. Rev. B **92**, 174113 (2015).
[24] L. J. Fetters, D. J. Lohse, D. Richter, T. A. Witten, and A. Zirkel, Macromolecules **27**, 4639 (1994).
[25] I. W. Gilmour, A. Trainor, and R. N. Haward, J. Appl. Polym. Sci. **23**, 3129 (1979).
[26] K. G. Lyon, G. L. Salinger, and C. A. Swenson, Phys. Rev. B **19**, 4231 (1979).
[27] J. Richeton, G. Schlatter, K. S. Vecchio, Y. Rémond, and S. Ahzi, Polymer **46**, 8194 (2005).
[28] C. M. Roland, Macromolecules **43**, 7875 (2010).
[29] J. L. Keddie, R. A. L. Jones, and R. A. Cory, Faraday Discuss. **98**, 219 (1994).
[30] J. L. Keddie, R. A. L. Jones, and R. A. Cory, Europhys. Lett. **27**, 59 (1994).
[31] J. A. Forrest, K. Dalnoki-Veress, J. R. Stevens, and J. R. Dutcher, Phys. Rev. Lett. **77**, 2002 (1996).
[32] J. A. Forrest and K. Dalnoki-Veress, Adv. Colloid Interface Sci. **94**, 167 (2001).
[33] S. Kawana and R. A. L. Jones, Phys. Rev. E **63**, 021501 (2001).
[34] A. N. Gent, J. Appl. Polym. Sci. **6**, 433 (1962).
[35] S. S. Sternstein and T. C. Ho, J. Appl. Phys. **43**, 4370 (1972).
[36] T. A. Tervoort, E. T. J. Klompen, and L. E. Govaert, J. Rheol. **40**, 779 (1996).
[37] C. M. Roland, Soft Matter **4**, 2316 (2008).
[38] I. M. Hodge, Science **267**, 1945 (1995).
[39] R. A. Barton, B. Ilic, A. M. Van Der Zande, W. S. Whitney, P. L. McEuen, J. M. Parpia, and H. G. Craighead, Nano Lett. **11**, 1232 (2011).